RSC Advances

PAPER

View Article Online
View Journal | View Issue

Cite this: *RSC Adv.*, 2025, **15**, 47946

Strain evolution and *in situ* phase transitions in freestanding $BaTiO_3$ epitaxial membranes *via* a $La_{2/3}Sr_{1/3}MnO_3$ sacrificial layer

K. Gurukrishna, [a] Aditya Uday Kamat,[a] Rishow Kumar,[a] Ashish Garg[b] and Shikhar Misra *[a]

Received 9th October 2025
Accepted 22nd November 2025

DOI: 10.1039/d5ra07695a

rsc.li/rsc-advances

Freestanding epitaxial thin films offer huge potential for flexible electronics and heterogeneous integration with next-generation devices. Herein, we successfully demonstrate the support-free lift-off of a single-crystalline $BaTiO_3$ (BTO) epilayer using a $La_{2/3}Sr_{1/3}MnO_3$ (LSMO) sacrificial layer deposited on a $SrTiO_3$ (001) single-crystalline substrate. The freestanding BTO membrane was heterogeneously integrated onto glass, enabling the study of the etched surface. With a *c*/*a* ratio of 1.005, the epitaxial BTO exhibited an out-of-plane compression with an in-plane tensile strain compared to the bulk counterparts, with an out-of-plane strain relaxation observed in the freestanding membrane compared to the epitaxial stacks. Surface characterization *via* X-ray photoelectron spectroscopy (XPS), atomic force microscopy (AFM), and optical profilometry confirms the structural and surface integrity. Temperature-dependent confocal Raman spectroscopy demonstrates *in situ* phase transitions in the freestanding BTO layer across the low- and high-temperature regimes (−170–200 °C). Overall, this work advances the heterogeneous integration of freestanding single-crystalline BTO membranes, providing critical insights into their strain-state evolution and temperature-dependent phase stability.

Introduction

Freestanding epitaxial thin films have opened new opportunities in flexible electronics and hetero-integration and have facilitated next-generation device design coexisting with current CMOS technologies[1] Such freestanding films can be integrated onto a variety of surfaces – including flexible polymers, semiconductor substrates or even curved topographies – enabling pathways for next-generation electronics, such as flexible displays, wearable sensors, and advanced biomedical devices[2] However, achieving high-quality single-crystalline freestanding membranes is often accompanied by the introduction of defects, thereby degrading their functional properties. However, recent advances in freestanding oxide technology enable the formation of high-quality single-crystalline materials without the constraints imposed by conventional rigid substrates.[3,4] Techniques for releasing single-crystalline layers include remote epitaxy,[5] where the growth is guided by the substrate's atomic potential through an ultrathin 2D spacer, enabling easy peel-off; selective substrate etching, which removes a parent or buried layer chemically or electrochemically to free the film;[6] and sacrificial-layer methods, which incorporate a dissolvable intermediate during growth that is later removed to release the high-quality crystal for transfer and heterogeneous integration.[7] The development of these freestanding films critically depends on the selection and thickness of an underlying sacrificial layer, and understanding their strain states and phase stability under varying conditions is essential for practical applications.

Among different perovskite oxides, $BaTiO_3$ (BTO) is particularly interesting due to its exceptional ferroelectric,[8] piezoelectric,[9] electro-optical[10] and nonlinear optical properties,[11] leading to its application in integrated electronic and optical devices. While BTO has been widely studied (both in bulk and thin film form), the properties of freestanding BTO membranes, particularly their strain relaxation and phase transitions, remain less explored. The heterogeneous integration of complex oxide freestanding membranes has been achieved using various sacrificial layers, such as BaO,[12] $La_{0.5}Sr_{0.5}MnO_3$, $La_{0.66}Sr_{0.33}MnO_3$ (LSMO),[13] $DSr_3Al_2O_6$ (SAO),[14–16] $SrCuO_2$ (SCO),[7] $SrMnO_3$ (ref. 17) and $SrVO_3$.[18] The fabrication of complex perovskite layers has been successfully demonstrated using various etching agents, notably acidic solutions and deionized water. In parallel, water-soluble sacrificial layers, like $Sr_3Al_2O_6$ and $Sr_4Al_2O_7$, have gained significant attention for their efficacy in facilitating layer-transfer processes.[16] The selection of a sacrificial layer is typically governed by two key factors: (i) minimal lattice mismatch with the substrate and functional layer and (ii) distinct chemical stability to enable selective etching. Among different sacrificial layers, LSMO exhibits

[a]*Department of Materials Science and Engineering, Indian Institute of Technology Kanpur, Kalyanpur, Kanpur 208016, UP, India. E-mail: shikharm@iitk.ac.in*
[b]*Department of Sustainable Energy Engineering, Indian Institute of Technology Kanpur, Kalyanpur, Kanpur 208016, UP, India*

superior strain adaptability, accommodating a wide range of epitaxial layers with varying lattice constants. Various materials, such as $SrRuO_3$,[19] $Hf_{0.5}Zr_{0.5}O_2$,[13] Pb $(Zr_{0.2}Ti_{0.8})O_3$ (PZT),[20] and $BaTiO_3$,[21,22] have been successfully fabricated using $La_{0.66}Sr_{0.33}MnO_3$ (LSMO) (with different La/Sr stoichiometries) as a sacrificial layer. LSMO offers distinct advantages for BTO lift-off due to its high crystalline coherence and minimal lattice mismatch. In addition, the etching rate of BTO is extremely low in the etchant solution (dilute HCl + KI) used for LSMO removal.[21] Recent studies demonstrate BTO lift-off *via* remote epitaxy, leveraging substrate potential through 2D layers.[5] Sacrificial-layer-assisted methods also enable clean release and transfer of BTO films onto diverse substrates. Recent studies highlight the detachment of BTO thin films from both perovskite substrates like $SrTiO_3$ (STO)[22] and non-perovskite substrates such as Al_2O_3,[23] followed by their transfer onto secondary platforms including glass, silicon, and flexible polymeric supports.

Previous studies on BTO freestanding membranes have mainly focused on using supporting layers such as PDMS or PMMA for mechanical transfer. Here, we carry out a detailed investigation of the structural and surface properties of the etched interface lifted off using sacrificial LSMO without a capping layer, which remains unexplored. In addition, the temperature-dependent phase transition behavior of BTO membranes needs further study. In this work, we demonstrate a successful support-free lift-off of the BTO epilayer using LSMO as a sacrificial layer. The freestanding BTO layer was heterogeneously integrated onto a glass substrate with the etched interface facing upward, on which the surface properties were analyzed. Further, *in situ* phase transitions across low and high temperatures (from −170–200 °C) were analyzed *via* Raman spectroscopy to systematically investigate phase transitions across a broad temperature range.

Materials and methods

Epitaxial heterostructures of $BaTiO_3$ (BTO)/$La_{2/3}Sr_{1/3}MnO_3$ (LSMO) are deposited on a $SrTiO_3$ (001) substrate using the pulsed laser deposition (PLD) method with a KrF excimer laser ($\lambda = 248$ nm). Both layers (LSMO and BTO) were deposited at an oxygen partial pressure of 0.133 mbar (base pressure $= 3 \times 10^{-6}$ mbar) and a substrate temperature of 600 °C. 4000 laser pulses of LSMO and BTO were deposited with a laser fluence of 2.0 J cm^{-2} at a repetition rate of 5 Hz. During the deposition, the laser beam is focused on the polycrystalline target covering an area of about 1 mm × 3 mm. The individual thicknesses of the LSMO and BTO layers are found to be ∼80 nm, as measured using a Bruker Dektak XT stylus profilometer. After the deposition, 30 min of *in situ* annealing was carried out at 600 °C, under an oxygen partial pressure of 0.133 mbar, followed by cooling to room temperature at a rate of 15 °C per minute. After confirming the phase formation, etching of the sacrificial LSMO layer was carried out. A solution consisting of diluted hydrochloric acid (HCl) with aqueous potassium iodide (KI) was used as an etchant at ambient temperature. The strength of the HCl solution used is 5%. 25 mg of KI was dissolved in 10 ml of DI water and mixed well to obtain a homogeneous solution. The etching process was monitored at different HCl and KI concentrations. Initially, the epitaxial LSMO layer grown on STO was immersed in the etchant solution to ensure proper etching of the sacrificial layer and to standardise the strength of the etchant. Then, the BTO/LSMO stack of epilayers was immersed in the etchant solution for 48 hours. After visually confirming the preferential etching of the sacrificial LSMO layer, the substrate with the BTO layer on it was removed carefully and slowly dipped in DI water so that the BTO layer floats on the water surface. The BTO layer was then flipped and transferred to the glass substrate using a homemade copper wire loop (to inhibit the surface tension). The entire process is shown schematically in Fig. 1. The membrane was about 3 × 3 mm in area. A photograph and optical microscopic image of the membrane are depicted in Fig. S2.

Epitaxial phase formation in all the samples was confirmed *via* X-ray diffraction (Panalytical Empyrean X-ray diffractometer) using Cu Kα radiation with a wavelength of 1.5406 Å. Ionic states in the as-grown films were investigated using X-ray photoelectron spectroscopy (PHI 5000 Versa Prob II, FEI. Inc.). To determine the elemental composition, scans were conducted from 0 to 1200 eV with a 0.8 eV resolution under ultrahigh vacuum. An Al Kα source with an energy of 1486 eV was used for X-ray generation. High-resolution spectra were taken at a step size of 0.05 eV at 50 milliseconds per step. The surface topography was visualised with a Bruker contour GT-K 3D optical profilometer. Morphology of the freestanding membrane was analysed using an Asylum Research MFP-3D atomic force microscope. *In situ* phase transition in the BTO membrane was observed using confocal Raman spectroscopy at low and high temperatures (Princeton Instruments-Acton Spectra Pro 2500i) equipped with a 532 nm DPSS laser (Laser Quantum gem) with 40 mW head power. The diameter of the laser spot is ∼2 μm at a zoom level of 50×. High-temperature measurements were carried out using a controlled heating stage T95-PE (AIRIX Corp), whereas low-temperature measurements up to −173 °C were carried out using a liquid nitrogen pump LNP95 (AIRIX Corp) at a controlled cooling rate.

Results and discussions

Initially, LSMO thin films were deposited on the STO (001) substrate, upon which the etching of the LSMO sacrificial layer was performed. Fig. 2a shows the θ–2θ XRD scans of LSMO/STO (001) before and after etching. The XRD graph clearly shows the absence of the (002) LSMO peak, thereby confirming the complete etching of the sacrificial layer. Further, BTO thin films were grown on the LSMO-buffered STO substrate, following which the etching of the LSMO layer was performed. The BTO membrane is transferred to the amorphous glass substrate, thereby demonstrating the preserved intrinsic crystalline quality of the original film despite the subsequent absence of atomic-scale order in the supporting substrate. The θ–2θ XRD scan and ϕ scans confirm the epitaxy of the as-grown heterostructure. As shown in Fig. S3, the normalized XRD (002) profiles of the BTO strained layer and membrane exhibit nearly

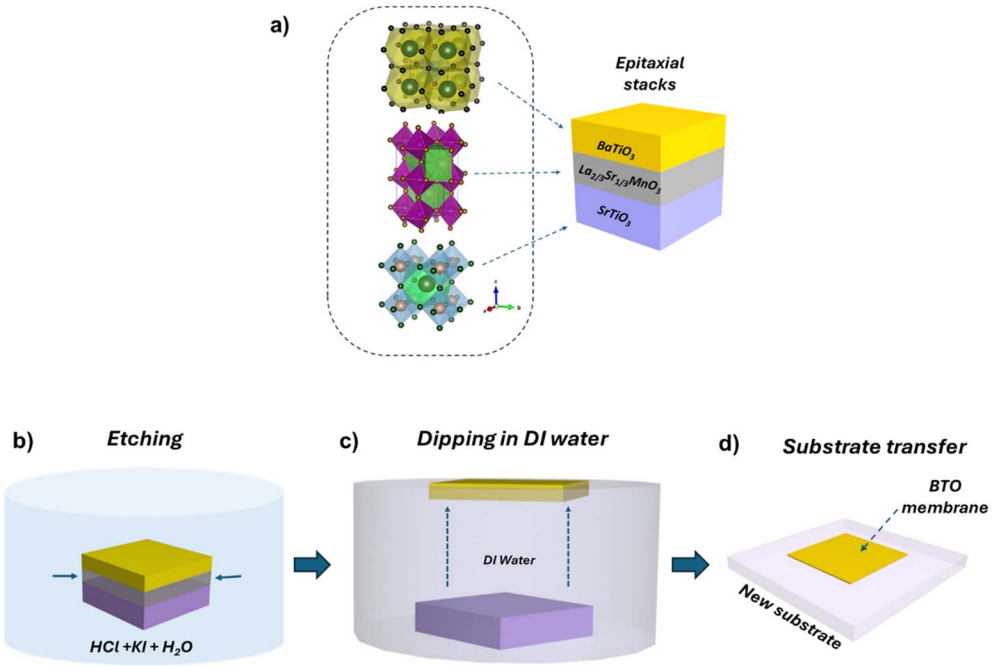

Fig. 1 Schematic representation of the steps involved in the lift-off of epitaxial BTO using a LSMO sacrificial layer. (a) Structure of the BTO/LSMO/STO thin film stacks deposited *via* PLD, (b) preferential etching of the LSMO sacrificial layer using a HCl + KI + H_2O solution, (c) dipping the membrane and substrate assembly in DI water and (d) transfer of the BTO membrane onto a glass substrate.

identical peak intensities, with a consistent FWHM of 0.485°. This confirms that the lift-off process does not compromise the crystallinity of the BTO layer. The dotted lines in Fig. 2b show the (002) reflection of BTO, which depicts a small lower-angle shift in the peak corresponding to the BTO membrane. The ϕ scan around the (103) reflection of the thin film stack is depicted in Fig. 2c. Four peaks separated by 90° show the four-fold symmetry of the epitaxial structures, indicating the cube-on-cube growth of BTO and LSMO on the STO substrate with no in-plane rotation (BTO[001]||LSMO[001]||STO[001] and BTO [100]||LSMO[100]||STO[100]), which is consistent with the previous reports.[24] Following the etching process,

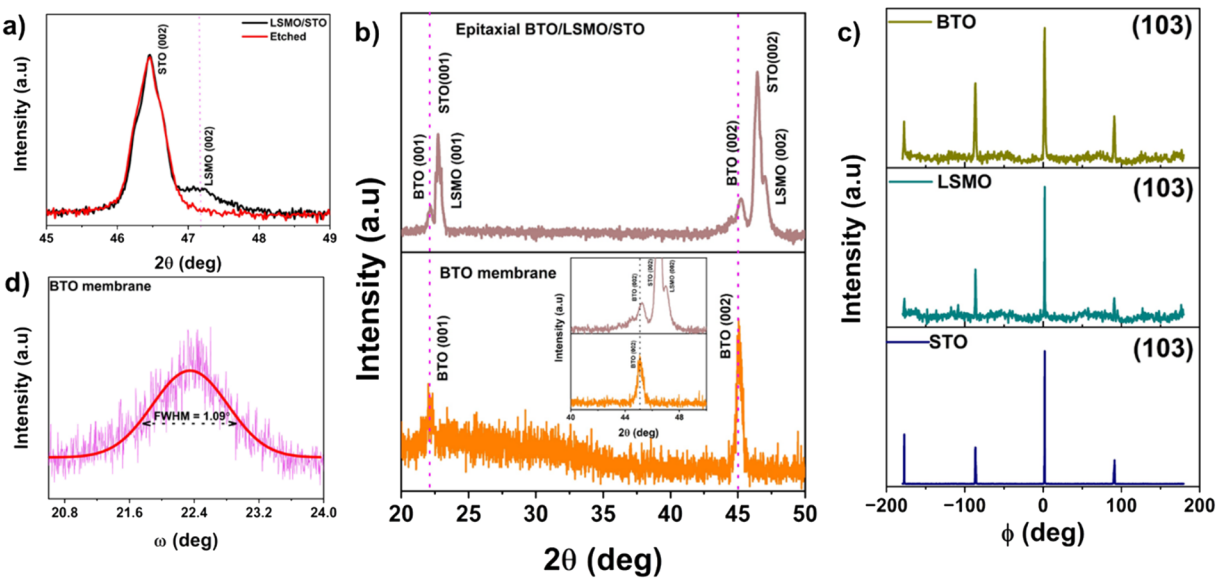

Fig. 2 (a) $\theta-2\theta$ XRD profile of LSMO/STO before and after etching, confirming the absence of the LSMO (002) peak upon etching, (b) $\theta-2\theta$ XRD profile of epitaxial stacks and freestanding BTO membrane depicting the presence and absence of the substrate with inset showing the zoomed part of the (002) reflection, (c) ϕ scans of epitaxial the BTO/LSMO/STO stacks around the (103) reflection, and (d) XRD rocking (ω) scan of the freestanding BTO membrane with FWHM of 1.09° on the glass substrate.

a freestanding BTO membrane on the glass substrate was obtained, upon which XRD was performed (shown in Fig. 2b). Monocrystalline (00l) reflections of BTO were found to be intact in the freestanding membrane over the glass substrate, preserving the single-crystalline nature of BTO. Rocking scan (ω) of the BTO membrane (Fig. 2d) fitted with a pseudo-Voigt function, shows a fair crystallinity with an FWHM of around 1.09°. Rocking curve of the BTO epilayer is shown in Fig. S3. FWHM of the spread in the strained BTO is observed to be 0.23, which suggests the slight decay of quality in the BTO membrane.

The 2D reciprocal space mapping (RSM) of the BTO/LSMO/STO shown in Fig. 3a shows distinct diffraction spots of BTO and LSMO on the STO (001) substrate, thus confirming the high epitaxial quality of these thin films. Fig. 3b shows the RSM acquired around the pseudo cubic (103) reflection of BTO/LSMO/STO, in which the out-of-plane components of the scattering vector Q_z (direction of growth) are plotted against the in-plane component Q_x associated with the [100] direction. The three main irregular spots in the maps correspond to the (103) pseudo cubic reflections of each layer of the heterostructure.[25] From reciprocal scattering vectors ($a = 2\pi/Q_x$), the out-of-plane lattice constant of the BTO epilayer is estimated to be $c = 4.027 \pm 0.001$ Å, whereas the in-plane lattice constant $a = 4.008 \pm 0.002$ Å. In comparison with the standard lattice constant of bulk BTO ($c = 4.033$ Å; $b = 3.991$ Å), the lattice distortions are found to be induced in the layers due to the epitaxial strain induced by the substrate.[26] The strain in the in-plane direction is evaluated using the formula $\varepsilon_a = \frac{a_{\text{film}} - a_{\text{bulk}}}{a_{\text{bulk}}} \times 100$, whereas the strain in out-of-plane direction is derived using $\varepsilon_c = \frac{C_{\text{film}} - C_{\text{bulk}}}{C_{\text{bulk}}} \times 100$. With a c/a ratio of 1.005, BTO exhibits an out-of-plane compression ($\varepsilon_c = -0.15\%$) with an in-plane tensile strain ($\varepsilon_a = +0.22\%$) as compared to the bulk counterparts. This out-of-plane compression strain is slightly relaxed ($\varepsilon_c = -0.10\%$) in the freestanding BTO membrane as seen from the symmetric RSM scan in Fig. 3c around the (002) reflection, from which the out-of-plane lattice constant of 4.029 ± 0.001 Å is derived. The relaxation of the strain in the out-of-plane direction is about 0.05% as compared to the clamped BTO film. The origin of the epitaxial strains can be related to the higher lattice mismatch between the LSMO and BTO layers.

The surface topography of the freestanding BTO membrane from the etched interface was studied with the help of optical profilometry as well as atomic force microscopy (AFM). Optical profilometry images (Fig. 4a) were taken across a larger area, which shows wrinkles at the micro level formed during the substrate transfer, essentially due to the absence of a support.[27] Micro-level patches were also observed, which were formed during the etching process in a corrosive solution across the interface. Fig. 4b and c show the AFM micrographs of the stacked BTO epilayer and BTO membranes at 2 × 2 μm areal scans. The RMS roughness of the strained BTO layer was found to be 4 nm. AFM micrographs of the strained BTO surface reveal a predominantly flat topography with the RMS surface roughness of about 4 nm. The surface morphology of the as-grown

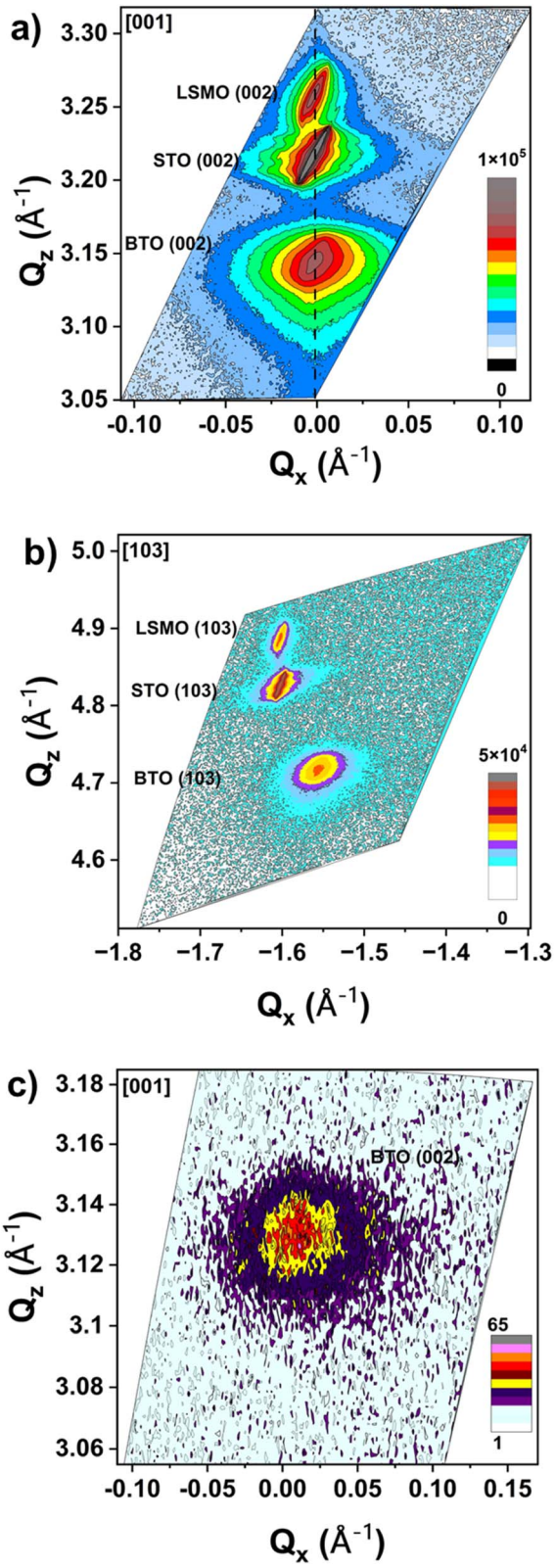

Fig. 3 (a) Symmetric RSM scans of the BTO/LSMO/STO stacks around the (002) reflection, (b) asymmetric RSM scans of the BTO/LSMO/STO stacks around the (103) reflection, and (c) symmetric RSM scans of the freestanding BTO membrane around the (002) reflection.

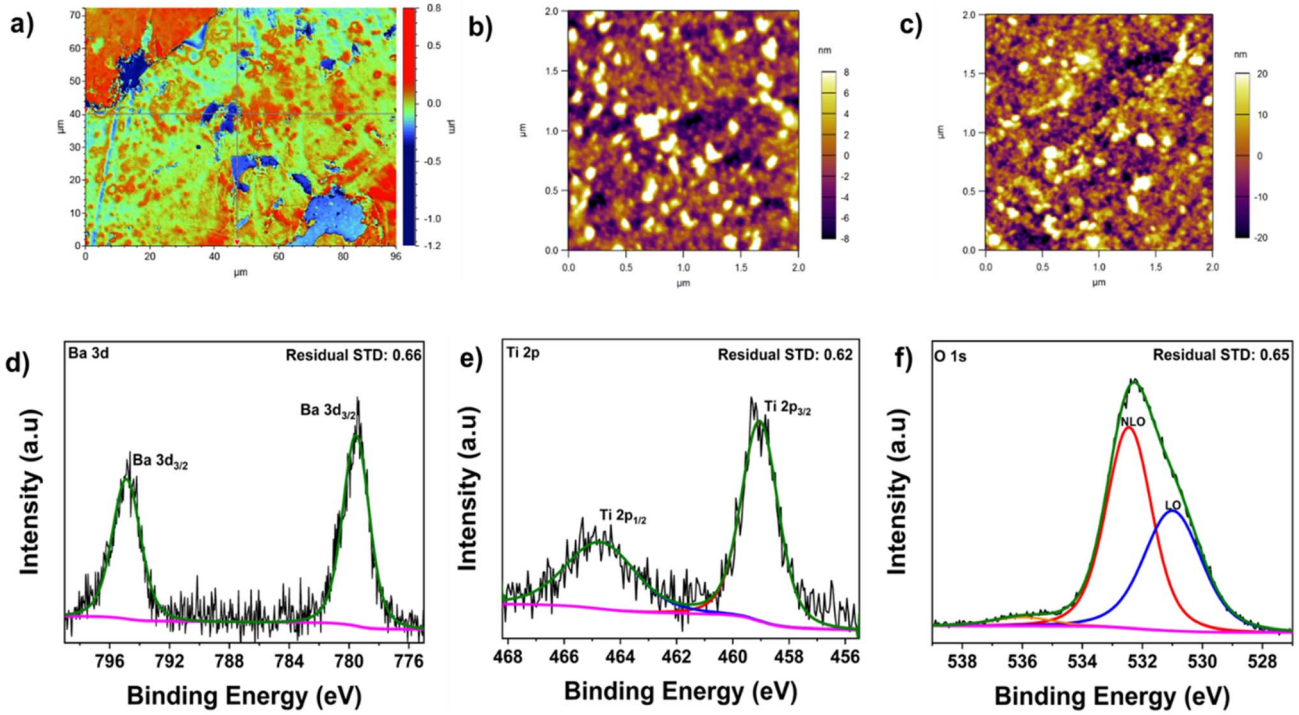

Fig. 4 (a) Surface topography of the BTO freestanding membrane by optical profilometry, (b) AFM micrograph of the BTO stacked epilayer and (c) AFM micrograph of the BTO membrane at the same areal scans. (d) Ba 3d core-level, (e) Ti 2p core-level, and (f) O 1s core-level XPS spectra of the BTO membranes fitted with a combination of Lorentzian and Gaussian functions.

films is known to be sensitive to both deposition kinetics and defect dynamics. In this study, due to a relatively high growth rate, which, in conjunction with solidification-related defect formation, likely contributed to increased surface roughness.[28,29] On the other hand, the surface roughness of the membrane was found to be 6 nm, depicting a small deterioration in surface morphology, mainly due to etching of the LSMO layer, causing inhomogeneity at the interface. AFM topography also suggests the existence of micro-level cracks and wrinkles on the membrane surface from the etched interface.

In the thin film stacks, the LSMO layer exhibits greater reactivity toward the etchant compared to the BTO layer. The etching of LSMO proceeds *via* the reduction of Mn ions and dissolution of La^{3+} and Sr^{2+} species into the solution as soluble chloride salts. The etchant concentration employed was insufficient to induce any significant chemical interaction with the BTO layer. To verify the absence of Ba and Ti chlorides at the etched interface, the membrane was flipped post lift-off to expose the etched surface, and XPS analysis was conducted. Local chemical environment of the freestanding layer was analyzed using XPS, as shown in Fig. 4d–f. The survey spectra of the BTO membrane are shown in Fig. S5. The spectra were calibrated as per the C 1s peak located at a binding energy of 284.6 eV. In the Ba core level, Ba $3d_{3/2}$ and $3d_{5/2}$ spin–orbit-splits were observed at 779.4 eV and 794.6 eV, respectively, with a doublet separation (ΔE) of 15.2 eV.[30] This is assigned to the Ba atoms in the perovskite structure. The symmetric doublets in the Ba core level reveal the existence of a single ionic state in the BTO membrane. The spin–orbit doublet peaks at 458.9 eV and 464.8 eV in the Ti core level belong to the Ti $2p_{3/2}$ and $2p_{1/2}$ levels, respectively, with a ΔE of 5.9 eV, which indicates the Ti^{4+} oxidation state. The symmetry of the $2p_{3/2}$ peak rules out the possibility of the Ti^{3+} ionic state in the sample.[9] The high-resolution O 1s spectra show a convoluted peak, which is deconvoluted into three parts *via* fitting with a combination of Gaussian–Lorentzian functions using CASA XPS software. The peak at a lower binding energy of 530.9 eV can be ascribed to the O–Ti–O binding state in the perovskite framework. The second part of the decomposed peak at 532.4 eV corresponds to the non-lattice oxygen, confirming the existence of oxygen vacancies ($V_o^{\cdot\cdot}$) in the sample. The third peak at 536.0 eV corresponds to the chemisorbed oxygen species.[31] Hence, XPS results confirm the purity of the BTO membrane, which does not exhibit any ionic states other than the recommended ones.

Finally, Raman spectroscopy was performed on the freestanding BTO layer to analyse the phase transition in different temperature regimes. The spectra were recorded using an excitation wavelength of 532 nm in the backscattered geometry. The sample was imaged *via* confocal microscope at a 50× zoom level with the focused laser spot diameter within 2 μm. Raman scattering was observed at a laser exposure time of 2 s with 20 accumulations. Temperature-dependent Raman spectra are illustrated in Fig. 5. In the tetragonal phase, T_{1u} vibrational modes split into A_1 and E modes, whereas the T_{2u} mode splits into B_1 and E phonon modes due to the non-centrosymmetricity of the structure. In general, the tetragonal phase of BTO is stable at near room temperatures (25–50 °C). At room temperature, the polar tetragonal BTO phase is present, which shows

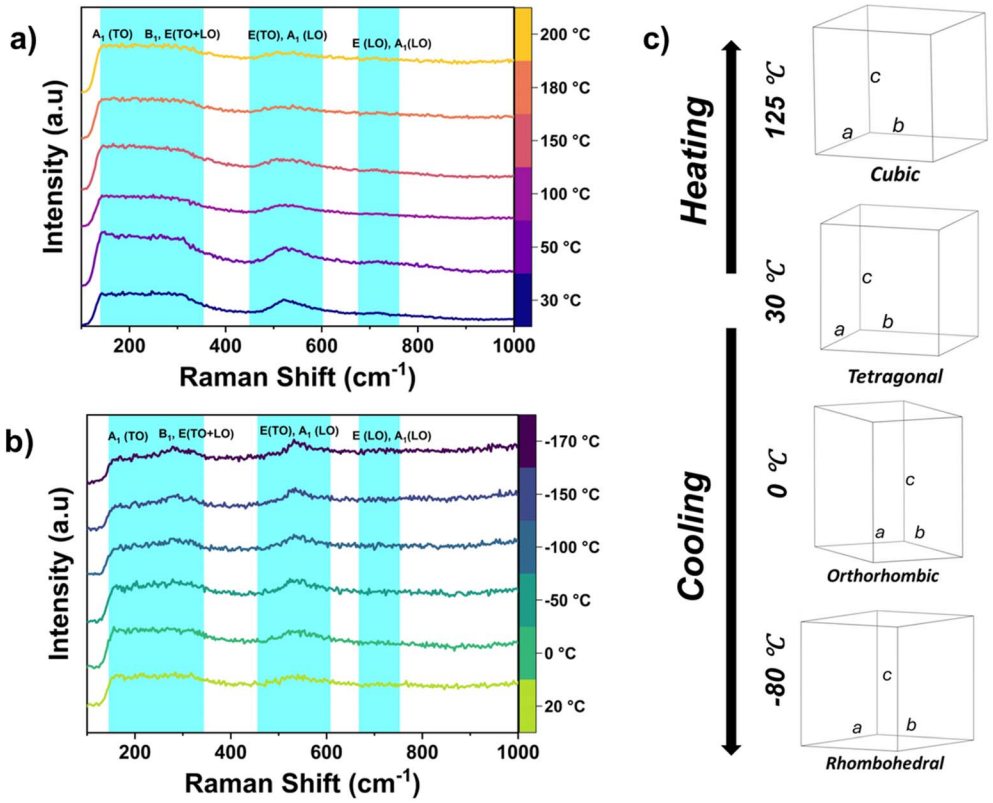

Fig. 5 Temperature-dependent Raman spectra of the freestanding BTO membrane (a) at high temperature (30 to 200 °C) and (b) at low temperature (30 to −170 °C) regimes. As the temperature increases, the A_1 + E(LO) mode is softened, whereas the A_1 + E(TO) mode shows a very broad band. As the temperature decreases, sharpening of the A_1(TO) peak is observed. The phase change in the freestanding BTO membrane is schematically shown in (c).

4E(TO + LO) + 3A_1(TO + LO) + B_1 Raman lattice vibration modes.[32] The Raman spectra at room temperature depict the bands at around 307 cm^{-1}, 521 cm^{-1}, and 715 cm^{-1}, confirming the tetragonal phase (4 mm symmetry)[33] At lower wave number ranges (180–300 cm^{-1}), the characteristic overlap of the A_1(TO) modes is observed due to the anti-resonance effect. The Raman band around 307 cm^{-1} corresponds to B_1 + E phonon modes, ascribing to the non-centrosymmetric regions appearing due to the displacement of Ti atoms in TiO_6 octahedra.[34] The asymmetric band across 521 cm^{-1} relates to the A_1 + E(TO) modes, whereas the A_1 + E(LO) mode causes the band centred around 715 cm^{-1}, which is considered the highest frequency longitudinal optical mode.[35] Fig. S6 in the SI depicts the Raman spectra of strained BTO and the membrane at ambient conditions. Nearly identical Raman modes are observed in both samples. In order to examine the phase transition from tetragonal to cubic, temperature-dependent Raman spectra were recorded from room temperature (30 °C) to 200 °C.[36] As the temperature increases above 50 °C, broadening of all Raman modes with lowered intensity is observed. At 200 °C, the overdamped A_1 + E(LO) mode is softened, whereas the A_1 + E(TO) mode shows a very broad band. Fig. S6 shows that the Raman mode at 521 cm^{-1} exhibits progressive broadening, with its full width at half maximum (FWHM) increasing from 68.0 cm^{-1} to 113.7 cm^{-1} as the temperature rises from 30 °C to 200 °C. Concurrently, the intensity ratio declines from 0.84 to 0.27. As the phase changes from tetragonal to cubic, the symmetry changes from C_{4v} (four-fold rotational axis and four vertical mirror planes) to O_h (octahedral) symmetry. Ideally, as per the selection rules, the cubic symmetry of BTO should be Raman inactive. However, the Raman modes are not entirely suppressed to yield a flat baseline, as reported in several studies. The tetragonal-to-cubic phase transition is interpreted within the framework of the order–disorder model. In the paraelectric (cubic) phase, Ti ions are randomly displaced along the cubic diagonals, in contrast to the ideal tetragonal perovskite structure, where Ti ions occupy the body-centred position. These local Ti displacements give rise to broad Raman bands above Tc, consistent with the observations by Ju *et al.*[37] and Marssi *et al.*[38] In the O_h symmetry of the cubic phase, the four optical modes transmute into a single T_{2u} and three T_{1u} irreducible representations.[37] Fig. 5b shows the evolution of Raman spectra at low temperatures in the cooling cycle. As the temperature goes below 0 °C, the FWHM of the A_1(TO) peak was found to decrease, indicating the transition from tetragonal to orthorhombic. As the temperature is reduced further, the A_1(TO) grows much sharper until −170 °C. Moreover, the Raman mode at 270 cm^{-1} was found to show up at higher intensities, along with the Raman mode at 307 cm^{-1}, which indicates the transition into a rhombohedral phase below −100 °C.[32,39] The

ferroelectric properties of the strained BTO film stack are given in Fig. S7.

Conclusion

This work demonstrated the successful lift-off of the epitaxial BTO layer *via* sacrificial LSMO-assisted lift-off. With a *c*/*a* ratio of 1.005, the epitaxial BTO was found to exhibit an out-of-plane compression with an in-plane tensile strain as compared to the bulk counterparts. A small out-of-plane strain relaxation is observed in the freestanding membrane in comparison with the epitaxial stacks. The existence of recommended ionic states and surface topography is inspected *via* XPS, AFM, and optical profilometry. *In situ* phase transition in the freestanding BTO layer is analysed across the low and high temperature regimes (−170–200 °C) *via* confocal Raman spectroscopy. The phase transition from tetragonal to cubic was witnessed at high temperatures above 125 °C. Tetragonal to orthorhombic (below 0 °C) and to rhombohedral (−80 °C) transitions were also witnessed at cryogenic temperatures. The current study is based on the release of the membrane without any support layers. To minimize defects, a PMMA stamp or a layer of PVA can be used in covering the functional layer. This can reduce the cracks during the transfer. This study opens opportunities to explore flexible electronics using a wide range of complex phase-change materials on versatile substrates, featuring various strain states and crystalline transformations, and also provides a material basis for designing freestanding flexible devices.

Conflicts of interest

The authors declare that they have no known competing financial interests or personal relationships that could have appeared to influence the work reported in this paper.

Data availability

The data can be made available from the corresponding author on reasonable request.

Supplementary information (SI): synthesis details, ferroelectric characterization, and other supporting data. See DOI: https://doi.org/10.1039/d5ra07695a.

Acknowledgements

GK would like to acknowledge the Institute Postdoctoral Fellowship (IPDF) grant for financial support. Authors would like to acknowledge the support from AOARD (FA2386-24-1-4027) and Kotak School of Sustainability, IIT Kanpur.

References

1 S. Puebla, T. Pucher, V. Rouco, G. Sanchez-Santolino, Y. Xie, V. Zamora, F. A. Cuellar, F. J. Mompean, C. Leon, J. O. Island, M. Garcia-Hernandez, J. Santamaria, C. Munuera and A. Castellanos-Gomez, Combining Freestanding Ferroelectric Perovskite Oxides with Two-Dimensional Semiconductors for High Performance Transistors, *Nano Lett.*, 2022, **22**, 7457–7466, DOI: 10.1021/acs.nanolett.2c02395.

2 S. Han, Y. Meng, Z. Xu, J. S. Kim, Y. Li, I. P. Roh, H. Ahn, D. H. Kim and S. H. Bae, Freestanding Membranes for Unique Functionality in Electronics, *ACS Appl. Electron. Mater.*, 2023, **5**, 690–704, DOI: 10.1021/acsaelm.2c01411.

3 R. Mandal, S. Yun, K. Wurster, E. Dollekamp, J. N. Shondo and N. Pryds, Recent Advancement in Ferroic Freestanding Oxide Nanomembranes, *Nano Lett.*, 2025, **25**, 5541–5549, DOI: 10.1021/acs.nanolett.5c00696.

4 D. S. Park and N. Pryds, The fabrication of freestanding complex oxide membranes: Can we avoid using water?, *J. Mater. Res.*, 2024, **39**, 2907–2917, DOI: 10.1557/s43578-024-01461-y.

5 L. Dai, J. Zhao, J. Li, B. Chen, S. Zhai, Z. Xue, Z. Di, B. Feng, Y. Sun, Y. Luo, M. Ma, J. Zhang, S. Ding, L. Zhao, Z. Jiang, W. Luo, Y. Quan, J. Schwarzkopf, T. Schroeder, Z. G. Ye, Y. H. Xie, W. Ren and G. Niu, Highly heterogeneous epitaxy of flexoelectric $BaTiO_{3-\delta}$ membrane on Ge, *Nat. Commun.*, 2022, **13**, 1–10, DOI: 10.1038/s41467-022-30724-7.

6 M. Lee, D. Mikulik and S. Park, The investigation of: In situ removal of Si substrates for freestanding GaN crystals by HVPE, *RSC Adv.*, 2018, **8**, 12310–12314, DOI: 10.1039/c8ra01347k.

7 M. Sheeraz, M. H. Jung, Y. K. Kim, N. J. Lee, S. Jeong, J. S. Choi, Y. J. Jo, S. Cho, I. W. Kim, Y. M. Kim, S. Kim, C. W. Ahn, S. M. Yang, H. Y. Jeong and T. H. Kim, Freestanding Oxide Membranes for Epitaxial Ferroelectric Heterojunctions, *ACS Nano*, 2023, **17**, 13510–13521, DOI: 10.1021/acsnano.3c01974.

8 G. Sánchez-Santolino, V. Rouco, S. Puebla, H. Aramberri, V. Zamora, M. Cabero, F. A. Cuellar, C. Munuera, F. Mompean, M. Garcia-Hernandez, A. Castellanos-Gomez, J. Íñiguez, C. Leon and J. Santamaria, A 2D ferroelectric vortex pattern in twisted $BaTiO_3$ freestanding layers, *Nature*, 2024, **626**, 529–534, DOI: 10.1038/s41586-023-06978-6.

9 S. K. Parate, S. Vura, S. Pal, U. Khandelwal, R. S. Sandilya Ventrapragada, R. K. Rai, S. H. Molleti, V. Kumar, G. Patil, M. Jain, A. Mallya, M. Ahmadi, B. Kooi, S. Avasthi, R. Ranjan, S. Raghavan, S. Chandorkar and P. Nukala, Giant electrostriction-like response from defective non-ferroelectric epitaxial $BaTiO_3$ integrated on Si (100), *Nat. Commun.*, 2024, **15**, 1428, DOI: 10.1038/s41467-024-45903-x.

10 H. Yu, N. Guo, C. Deng, H. Han, W. Li, C. Lebudi, S. Wang, Y. Li, Y. Chen, S. Peng, J. Zhang, J. Ma, Q. Zheng, J. Li and Q. Li, Tuning the Electro-Optic Properties of $BaTiO_3$ Epitaxial Thin Films via Buffer Layer-Controlled Polarization Rotation Paths, *Adv. Funct. Mater.*, 2024, **34**, 2315579, DOI: 10.1002/adfm.202315579.

11 Y. Wen, Y. Cao, H. Chen, X. Du, J. Guo, J. Shen, F. Zhang, T. Bian, Y. An, H. Ren, Z. Wu, W. Liu and Y. Zhang, Enhanced Electro-Optic Coefficients in Single-Crystalline $BaTiO_3$ Thin Films Enabled by Domain Alignment, *Adv. Opt. Mater.*, 2024, **12**, 2303058, DOI: 10.1002/adom.202303058.

12 R. Takahashi and M. Lippmaa, Sacrificial Water-Soluble BaO Layer for Fabricating Free-Standing Piezoelectric Membranes, *ACS Appl. Mater. Interfaces*, 2020, **12**, 25042–25049, DOI: 10.1021/acsami.0c05830.

13 Y. C. Liu, B. C. Chen, C. C. Wei, S. Z. Ho, Y. De Liou, P. Kaur, N. Rahul, Y. C. Chen and J. C. Yang, Thickness-Dependent Ferroelectricity in Freestanding $Hf_{0.5}Zr_{0.5}O_2$ Membranes, *ACS Appl. Electron. Mater.*, 2023, **6**, 8617–8625, DOI: 10.1021/acsaelm.3c01856.

14 D. Ji, S. Cai, T. R. Paudel, H. Sun, C. Zhang, L. Han, Y. Wei, Y. Zang, M. Gu, Y. Zhang, W. Gao, H. Huyan, W. Guo, D. Wu, Z. Gu, E. Y. Tsymbal, P. Wang, Y. Nie and X. Pan, Freestanding crystalline oxide perovskites down to the monolayer limit, *Nature*, 2019, **570**, 87–90, DOI: 10.1038/s41586-019-1255-7.

15 Q. Wang, J. Wang, H. Fang, Y. Chen, Y. Han, H. Liu, D. Wang, P. Zhang, C. Shi, J. Guo, B. He, L. Zheng and W. Lü, Polarization Evolution in Morphology-Engineered Freestanding Single-Crystalline $BaTiO_3$ Membranes, *J. Phys. Chem. C*, 2022, **126**, 16369–16376, DOI: 10.1021/acs.jpcc.2c04404.

16 D. Lu, D. J. Baek, S. S. Hong, L. F. Kourkoutis, Y. Hikita and H. Y. Hwang, Synthesis of freestanding single-crystal perovskite films and heterostructures by etching of sacrificial water-soluble layers, *Nat. Mater.*, 2016, **15**, 1255–1260, DOI: 10.1038/nmat4749.

17 Y. Cai, Y. T. Xu, M. Y. Fu, M. Feng, H. Y. Peng, Y. F. Jiang, B. W. Wang, Y. Q. Wang, Z. Guan, B. Bin Chen, N. Zhong, C. G. Duan and P. H. Xiang, Superior Strain-Adapted Sacrificial Layer for the Synthesis of Freestanding Perovskite Oxide Films, *ACS Appl. Mater. Interfaces*, 2025, **17**, 21459–21468, DOI: 10.1021/acsami.5c01102.

18 Y. Bourlier, B. Bérini, M. Frégnaux, A. Fouchet, D. Aureau and Y. Dumont, Transfer of Epitaxial $SrTiO_3$ Nanothick Layers Using Water-Soluble Sacrificial Perovskite Oxides, *ACS Appl. Mater. Interfaces*, 2020, **12**, 8466–8474, DOI: 10.1021/acsami.9b21047.

19 R. Qiu, B. Peng, H. Liu, Y. Guo, H. Tang, Z. Zhou and M. Liu, Epitaxial growth of pure $Sr_3Al_2O_6$ sacrificial layer for high quality freestanding single-crystalline oxide membranes, *Thin Solid Films*, 2023, **773**, 139820, DOI: 10.1016/j.tsf.2023.139820.

20 S. R. Bakaul, C. R. Serrao, M. Lee, C. W. Yeung, A. Sarker, S. Hsu, A. K. Yadav, L. Dedon, L. You, A. I. Khan, J. D. Clarkson, C. Hu, R. Ramesh and S. Salahuddin, Single crystal functional oxides on silicon, *Nat. Commun.*, 2016, **7**, 10547, DOI: 10.1038/ncomms10547.

21 D. Pesquera, E. Parsonnet, A. Qualls, R. Xu, A. J. Gubser, J. Kim, Y. Jiang, G. Velarde, Y. Huang, H. Y. Hwang, R. Ramesh and L. W. Martin, Beyond Substrates: Strain Engineering of Ferroelectric Membranes, *Adv. Mater.*, 2020, **32**, 1–9, DOI: 10.1002/adma.202003780.

22 A. Haque, H. J. D'Souza, S. K. Parate, R. S. Sandilya, S. Raghavan and P. Nukala, Heterogeneous Integration of High Endurance Ferroelectric and Piezoelectric Epitaxial $BaTiO_3$ Devices on Si, *Adv. Funct. Mater.*, 2024, 2413515, DOI: 10.1002/adfm.202413515.

23 W. Zhou, D. Chen, R. Mitsuya, H. Ohta and T. Katayama, Millimeter-Sized Epitaxial Ferroelectric BaTiO3 Freestanding Sheets Peeled from Al_2O_3 Substrates, *ACS Appl. Electron. Mater.*, 2025, **7**, 4552–4556, DOI: 10.1021/acsaelm.5c00411.

24 S. N. Vayalil, S. Kumar and P. Murugavel, Flexo-Photovoltaic Effect in a Bandgap-Engineered Ferroelectric $BaTiO_3$ -Based Epitaxial Thin Film, *ACS Appl. Electron. Mater.*, 2025, **7**, 3837–3847, DOI: 10.1021/acsaelm.5c00113.

25 Y. Cao, Y. Wen, Y. Yang, F. Zhang, W. Zhang, J. Du, Y. Zhang, Z. Wu and J. Wu, Low-temperature growth of epitaxial $BaTiO_3$ thin films with significant electro-optic coefficients, *Appl. Phys. Lett.*, 2025, **126**, 111104, DOI: 10.1063/5.0237644.

26 Z. Liang, J. Wang, X. Liu, C. Li and X. Du, Strain-driven high energy storage in $BaTiO_3$-based lead-free epitaxial thin films, *Appl. Phys. Lett.*, 2024, **124**, 213903, DOI: 10.1063/5.0210053.

27 B. Zhang, C. Yun and J. L. MacManus-Driscoll, High Yield Transfer of Clean Large-Area Epitaxial Oxide Thin Films, *Nano-Micro Lett.*, 2021, **13**, 39, DOI: 10.1007/s40820-020-00573-4.

28 B. Shin and M. J. Aziz, Kinetic-energy induced smoothening and delay of epitaxial breakdown in pulsed-laser deposition, *Phys. Rev. B: Condens. Matter Mater. Phys.*, 2007, **76**, 08531, DOI: 10.1103/PhysRevB.76.085431.

29 P. S. Shewale, S. H. Lee and Y. S. Yu, Pulse repetition rate dependent structural, surface morphological and optoelectronic properties of Ga-doped ZnO thin films grown by pulsed laser deposition, *J. Alloys Compd.*, 2017, **725**, 1106–1114, DOI: 10.1016/j.jallcom.2017.07.269.

30 I. Spasojevic, G. Sauthier, J. M. Caicedo, A. Verdaguer and N. Domingo, Oxidation processes at the surface of BaTiO3 thin films under environmental conditions, *Appl. Surf. Sci.*, 2021, **565**, 150288, DOI: 10.1016/j.apsusc.2021.150288.

31 C. Blaess, S. Matzen, H. Lin, H. Magnan, J.-B. Moussy, C. L. Rountree, C. Mocuta, M. G. Silly, O. Plantevin, F. Charra and A. Barbier, Nitrogen Doping in Epitaxial Self-Oxidized $BaTiO_3$ Ferroelectric Thin Films, *J. Phys. Chem. C*, 2025, **129**, 3849–3861, DOI: 10.1021/acs.jpcc.4c07538.

32 Y. Zheng, Y. Zhao, J. Yu, W. Lu, J. Ning and C. Zheng, Temperature evolution of the Fano line shape in the Raman spectra of $BaTiO_3$ nanoparticles, *Appl. Phys. Express*, 2023, **16**, 032003, DOI: 10.35848/1882-0786/acc1be.

33 V. R. Nallagatla, C. Maier, J. Glettler, A. Feteira, K. Reichmann and M. Deluca, Synergistic homovalent and heterovalent substitution effects on piezoelectric and relaxor behavior in lead-free $BaTiO_3$ ceramics, *J. Eur. Ceram. Soc.*, 2024, **44**, 116689, DOI: 10.1016/j.jeurceramsoc.2024.116689.

34 Q. Sun, Q. Gu, K. Zhu, R. Jin, J. Liu, J. Wang and J. Qiu, Crystalline Structure, Defect Chemistry and Room Temperature Colossal Permittivity of Nd-doped Barium Titanate, *Sci. Rep.*, 2017, **7**, 1–8, DOI: 10.1038/srep42274.

35 M. Jauhari, S. K. Mishra, H. K. Poswal, R. Mittal and S. L. Chaplot, Evidence of low-temperature phase transition in $BaTiO_3$ -modified $NaNbO_3$: Raman spectroscopy study, *J. Raman Spectrosc.*, 2019, **50**, 1949–1955, DOI: 10.1002/jrs.5739.

36 A. Gajović, J. V. Pleština, K. Žagar, M. Plodinec, S. Šturm and M. Čeh, Temperature-dependent Raman spectroscopy of $BaTiO_3$ nanorods synthesized by using a template-assisted sol–gel procedure, *J. Raman Spectrosc.*, 2013, **44**(3), 412–420.

37 L. Ju, T. Sabergharesou, K. G. Stamplecoskie, M. Hegde, T. Wang, N. A. Combe, H. Wu and P. V. Radovanovic, Interplay between Size, Composition, and Phase Transition of Nanocrystalline Cr^{3+} -Doped $BaTiO_3$ as a Path to Multiferroism in Perovskite-Type Oxides, *J. Am. Chem. Soc.*, 2012, **134**, 1136–1146, DOI: 10.1021/ja2091678.

38 M. El Marssi, F. Le Marrec, I. A. Lukyanchuk and M. G. Karkut, Ferroelectric transition in an epitaxial barium titanate thin film: Raman spectroscopy and X-ray diffraction study, *J. Appl. Phys.*, 2003, **94**, 3307–3312, DOI: 10.1063/1.1596720.

39 Y. I. Yuzyuk, Raman scattering spectra of ceramics, films, and superlattices of ferroelectric perovskites: A review, *Phys. Solid State*, 2012, **54**, 1026–1059, DOI: 10.1134/S1063783412050502.